Ecological Indicators 141 (2022) 109102

Contents lists available at ScienceDirect

Ecological Indicators

journal homepage: www.elsevier.com/locate/ecolind

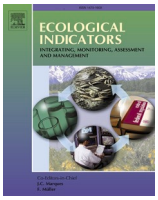

Original Articles

# Estimating grassland vegetation cover with remote sensing: A comparison between Landsat-8, Sentinel-2 and PlanetScope imagery

Davide Andreatta [a,b,*,1], Damiano Gianelle [b,2], Michele Scotton [a,3], Michele Dalponte [b,4]

[a] Department of Agronomy, Food, Natural Resources, Animals and Environment, University of Padova, Legnaro, Padova, Italy
[b] Research and Innovation Centre, Fondazione Edmund Mach, San Michele all'Adige, Trento, Italy

ARTICLE INFO

*Keywords:*
Erosion
Restoration
Spectral signature
Image classification
Fractional response model
Biophysical parameter retrieval

ABSTRACT

Grassland fractional vegetation cover (FVC) accurate mapping on a large scale is crucial, since degraded grasslands contribute less to provisioning services, carbon storage, water purification, erosion control and biodiversity conservation. The spatial and temporal resolution of Sentinel-2 (S2) and PlanetScope (PS) data has never been explored for grassland FVC estimation so far and will enable researchers and agencies to quantify and map timelier and more precisely grassland processes. In this paper we compare FVC estimation models developed from Landsat-8 (L8), S2 and PS imagery. The reference grassland FVC dataset was obtained on the Paganella ski runs (46.15°N, 11.01°E, Italy) applying unsupervised classification to nadir grassland RGB photographs taken from 1.35 m above the soil. Fractional Response Models between reference FVC and 18 vegetation indices (VIs) extracted from satellite imagery were fitted and analysed. Then, leave-one-out cross validation and spatiotemporal change analysis were also performed. Our study confirms the robustness of the commonly used VIs based on the difference between NIR and the red wavelength region ($R^2 = 0.91$ for EVI using S2 imagery) and indicate that VIs based on the red-edge spectral region are the best performing for PS imagery ($R^2 = 0.89$ for RECI). Only medium to high spatial resolution imagery (S2 and PS) precisely mapped spatial patterns at the study site, since grasslands FVC varies at a fine scale. Previously available imagery at medium to low spatial and temporal resolution (e.g., L8) may still be interesting for analysis requiring long time-series of data.

## 1. Introduction

Grassland degradation is a crucial issue, as degraded grasslands not only contribute less to provisioning services, but also to carbon storage, water purification, erosion control, biodiversity conservation, and recreation (Li et al., 2022). Grasslands cover one-third of the earth's terrestrial surface, which represent 70% of the global agricultural area (Reynolds and Frame, 2005), and over 49% of grassland area is experiencing these processes (Gang et al., 2014).

Grassland Fractional Vegetation Cover (FVC), defined as the ratio of the vertical projection area of above-ground vegetation organs on the ground to the total vegetation area, is a very informative trait in grassland monitoring (Liang and Wang, 2020). Spatiotemporal changes in FVC reflect changes in grasslands functioning caused by environmental drivers such as erosion, revegetation, alteration of disturbance regimes, precipitation and temperature patterns.

FVC estimation is mainly performed using two approaches: field measurements and remote sensing retrieval. In the field, FVC measurement has been traditionally carried out using subjective methods like visual estimation, or more standardized sampling methods like the grid method and the point count sampling method (Liang and Wang, 2020). Thanks to the improvements in image quality, digital photography classification became a much more efficient way of FVC estimation in the field, because it is fast, replicable and objective (Booth et al., 2005; Li et al., 2005). Supervised methods (also known as manual pixel classification) and unsupervised methods (also known as automatic colour threshold) have been developed to classify each pixel (Booth et al., 2006; McCallum, 2000; Patrignani and Ochsner, 2015; Zhou et al., 1998).

* Corresponding author at: Via dei Giardini, 27/1, 38122 Trento, Italy.
*E-mail address:* davide.andreatta@phd.unipd.it (D. Andreatta).
[1] ORCID: 0000-0001-6821-1152.
[2] ORCID: 0000-0001-7697-5793.
[3] ORCID: 0000-0002-0221-0875.
[4] ORCID: 0000-0001-9850-8985.

https://doi.org/10.1016/j.ecolind.2022.109102
Received 2 May 2022; Received in revised form 20 June 2022; Accepted 22 June 2022

Field methods are still fundamental as they provide accurate ground reference measurement for remote sensing algorithm development, which has become the most used approach in FVC estimation for large scale applications (Liang and Wang, 2020; White et al., 2000).

The most common methods proposed for FVC estimation using RS data are i) empirical model methods (also called *regression models*), ii) pixel decomposition model methods (also called *linear unmixing model*), iii) physical based methods, and iv) machine learning methods. Empirical models are constructed through the regression of remote sensing data, which can be waveband values or derived VIs, to reference FVC values. Empirical models have been successfully explored since the experience of Graetz et al. (1988) who predicted FVC using the fifth channel of Landsat MSS at a spatial resolution of 183 m reaching an accuracy of $R^2 = 0.68$. The major drawback of regression models is they are locally calibrated, and they do not necessarily generalize well. The theoretical basis of the second approach, pixel decomposition models, is that each pixel in an image is composed of several components and pixel reflectance to the sensors is assumed to result from the linear synthesis of the information of each component. The pixel decomposition methods having just two endmembers, i.e. soil and vegetation, are also called pixel dichotomy models, dimidiate pixel models, or two-endmember models and compute the FVC considering the contribution of the vegetation component (maximum VI value) and of the bare soil (minimum VI value) (Gao et al., 2020; van der Meer, 1999). The physical-based methods simulate the physical relationships between vegetation canopy spectral reflectance and FVC, and the estimation is applied by inverting a canopy radiative transfer model (CRTM). One frequent issue using these algorithms is that the input parameters are often more than the observations, thus the equation is underdetermined (Atzberger, 2004; Darvishzadeh et al., 2008). For this reason, Machine Learning algorithms are often employed to constrain and simplify the inversion process (Baret et al., 2007; Roujean and Lacaze, 2002).

The spatial resolution of images used in FVC estimation are mainly from medium to coarse, with dominant values of 30 m, 250 m, 1 km (Gao et al., 2020). The most frequently used satellite imageries are, respectively, Landsat, MODIS, and AVHRR. Most of VIs used for FVC estimation are computed based on reflectances in the red and near-infrared (NIR) wavelength region, like the SAVI used by McGwire et al. (2000), MSAVI used by Chen et al. (2016), the EVI used by Jia et al. (2017), the WDRVI used by Gitelson (2013). Also the short-wave-infrared (SWIR) wavelength region showed correlation with FVC according to Guerschman et al. (2009) and to Baret et al. (2007). High correlations were found also with the red-edge, as reported by Gitelson (2013) and Liu et al. (2007) and with the green band (Zarei et al., 2020). Only a few studies explored the use of Sentinel-2 (S2) imagery for crop FVC estimation and to our knowledge grassland FVC estimation using S2 imagery has never been tested. Verrelst et al. (2012) simulated Sentinel-2 Multi spectral Instrument band settings on the basis of Compact High Resolution Imaging Spectrometry data to estimate the FVC of 8 crops, whereas Wang et al. (2018) applied a machine learning approach to estimate FVC of maize and wheat fields using S2 imagery. S2 imagery compared to previous imagery like Landsat-8 (L8) series benefits from improved spatial and spectral resolution, with RGB and NIR bands at 10 m, 4 red-edge bands (which were not available in the L8 series) and 2 shortwave infrared bands at 20 m. One last constellation that to our knowledge has never been tested for FVC estimation is PlanetScope (PS) constellation. The last instrument generation, PSB.SD, is capable of measuring reflectances in 8 bands at the high spatial resolution of about 3 m and with a nearly daily revisiting time.

Although the possibility to use spaceborne optical imagery at coarse resolution to estimate grassland FVC have already been explored in previous works, newly available imagery with finer spatial and spectral resolution could give much more detailed information, necessary to monitor patchy processes like grassland degradation and restoration that the global change is causing (Jia et al., 2017). Especially, S2 and PS imagery has never been applied to grassland FVC estimation, even though the higher spectral, spatial and temporal resolution may lead to breakthrough innovation in FVC estimation algorithms, especially in environments where vegetation mosaic changes at a fine scale (Gao et al., 2020). The output models could be used to monitor grassland degradation and recovery and to estimate grassland density changes in response to climate change.

In this work we aim to i) shed light on the sensitivity of spectral regions to changes in FVC and ii) to compare the FVC prediction capability of models developed using different optical imagery.

## 2. Materials and methods

### 2.1. Study area

The study was conducted at the southern border of the Italian Alps, in the Province of Trento, on the Paganella ski runs (46.15°N, 11.01°E, Fig. 1A). The climate of the study site is classified as temperate oceanic supratemperate humid according to the Worldwide Bioclimatic Classification System (Sboarina and Cescatti, 2004). The rains are concentrated in summer and autumn and annual precipitation is 1508 mm. The study area altitude ranges from 1055 m a.s.l. to 1615 m a.s.l. and the temperatures registered at the nearest (Fig. 1C) weather station (1790 m a.s.l.) reach their maximum in August (average of daily maximum = 18.1 °C) and their minimum in January (average of daily minimum = -7.3 °C) (Fig. 1B). The dominant plant communities in the study area are montane and subalpine spruce forests, interrupted by ski runs revegetated from more than 70 year to one year before our field survey. Commercial seed mixtures used for revegetation were mainly composed of *Festuca rubra, Dactylis glomerata, Lolium perenne, Trifolium repens, Trifolium pratense.* Based on the age of the revegetation and on soil conditions the FVC ranges from very low to complete in the surveyed grasslands.

### 2.2. Ground measurements of reference FVC

To construct our FVC ground measurement reference dataset, the digital photography approach was chosen (Liang and Wang, 2020). First, we identified 46 vegetationally homogeneous areas inside the grassland areas and we defined 10 m × 10 m plots with north orientation. The plots were georeferenced with a total station. Then, in each plot we took one Nadir photograph at the plot centre and one at each corner. The photographs were taken using a RGB digital camera mounted on a tripod 1.35 m above ground level. The camera was oriented vertically downwards resulting in a field view of approximately 120 cm × 100 cm, varying based on the slope. All images were obtained in a 4608 × 3456 pixels spatial resolution with flash always off and without optical or digital zoom. The field work was conducted between June 23 and 24, 2021 and resulted in 230 photographs.

To limit image edge distortion, image edges were removed (20% of height and 20% of width) before classification. We chose the unsupervised image classification method proposed by Patrignani and Ochsner (2015). This method detects the green pixels based on colour ratios of red to green (R/G) and blue to green (B/G) and on the excess green index (2G-R-B). The green pixels can be detected by the following criteria:

$$\frac{R}{G} < P_1 and \frac{B}{G} < P_2 and 2G - R - B < P_3 \quad (1)$$

where R is the red band, G is the green band, B is the blue band and P1, P2, and P3 are three parameters set to 0.95, 0.95, 20 by default. The method was chosen because it has been already successfully used to estimate grassland FVC (Jáuregui et al., 2019; Lollato et al., 2019). The parameters were set to the default values and the classification was performed using *R* (RStudio Team, 2020) (Fig. S1). Plot FVC was computed as the average FVC of the 5 photographs. Digital images classification provided a reference dataset composed of 15 plots in the

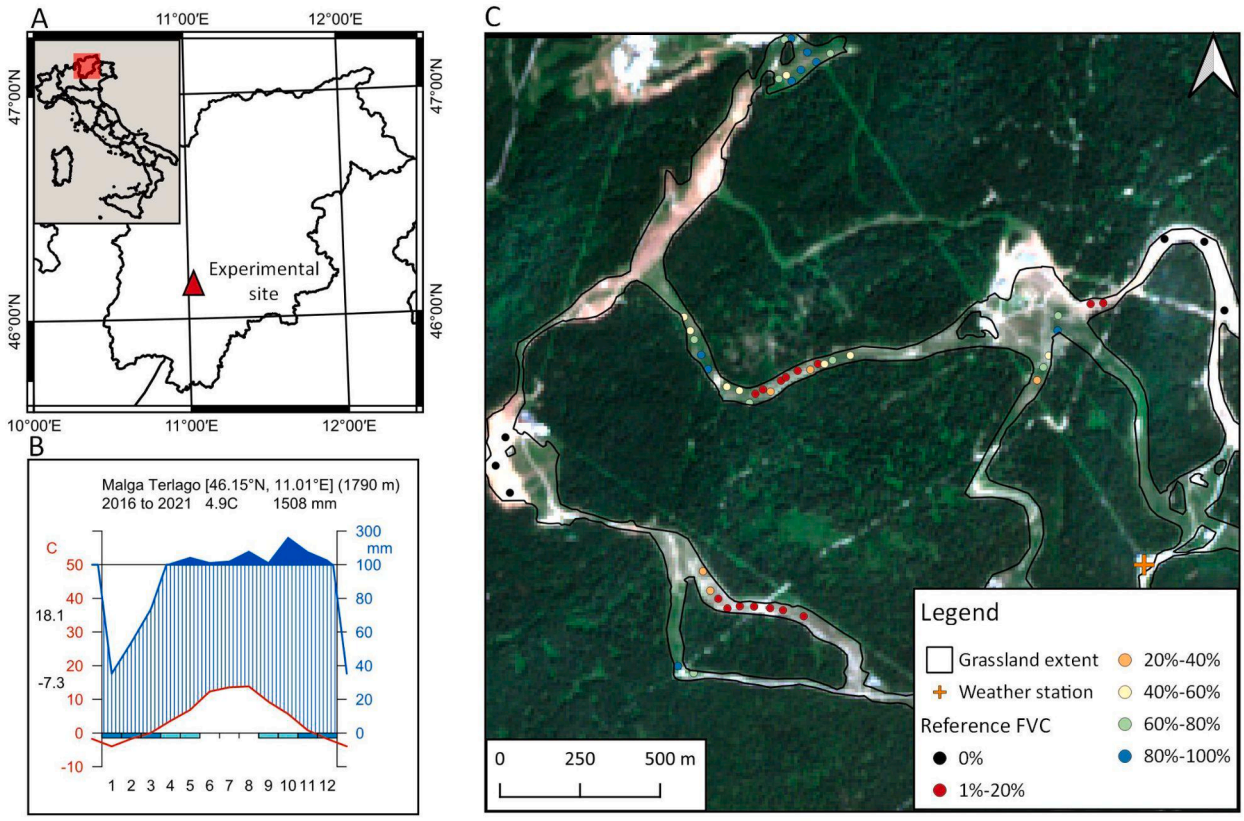


**Fig. 1.** A) Location of the experimental site. B) Walter & Lieth climatic diagram of the Malga Terlago weather station. Data downloaded from the weather service of the Province of Trento (www.meteotrentino.it). C) Plot Location inside the study site coloured based on their reference Fractional Vegetation Cover. Sentinel-2 Level 2A image of June 27th 2021 used as a background.

FVC range between 1% and 20%, 5 plots between 20% and 40%, 8 plots between 40% and 60%, 9 plots between 60% and 80% and 9 plots between 80% and 100%. The average standard deviations of reference FVC among subplots of each plot is 8.8 % (min = 1%, max 25%). Seven bare soil plots were also added to the dataset. In those plots the vegetation, most of the organic soil and rocks had been removed, and soil levelled for new ski runs preparation. Bare soil plots were included in the dataset to represent eroded grasslands rich in mineral soil, and to represent restored grasslands in their first stages after soil preparation.

### 2.3. Remote sensing imagery

For each imagery we identified the uncloudy image closest to the field survey dates (23rd and 24th June 2021), and product specification can be found in Table S1. Imagery from L8 constellation (13th of June 2021, Level 2) and S2 constellation (27th of June 2021, Level-2A) were accessed through the Earth Engine Data Catalog (https://developers.google.com/earth-engine/datasets) (Gorelick et al., 2017), whereas the PS image (23rd of June 2021, Level 3A, PSB.SD instrument) was download from the Planet API and then uploaded to the Earth Engine Code Editor for the sampling. Values of all the pixels that intersect the plots, weighted on the plot fraction intersected, were extracted for each band for the 53 plots (10 m × 10 m squares) using the *ee.Image.reduceRegions* function in Google Earth Engine. To produce the estimated FVC maps used for spatiotemporal change analysis (Fig. 5 and Fig. 6), the PS images at full resolution (3 m × 3 m) were spatially smoothed using 3 × 3 pixels moving window and assigning the mean values of the neighbourhood to the focal cell to match the calibration resolution (10 m × 10 m) without losing the fine scale detail. The *focal* function of the *raster* package in R was used to apply the spatial smoothing (Hijmans, 2021).

For the temporal change analysis described in subsection 2.7 and 3.3, four clear-sky images taken from summer to autumn 2021, were acquired for each imagery (dates reported in Fig. 6).

### 2.4. Vegetation index computing

The VIs included in this study were chosen based on previous literature. We included indices which analyse the NIR wavelength region (Chen et al., 2016; Jia et al., 2017; Jiménez-Muñoz et al., 2009), the SWIR (Baret et al., 2007; Guerschman et al., 2009) and the red-edge (Gao et al., 2020). Two indices exploring the green wavelength were also included, as they were successfully used for approximating gross primary productivity of grasslands (Zhou et al., 2014). The VIs were computed for each imagery in *R* using the formulas described in Table 1. It was not possible to compute all the VIs for all the imageries, since red-edge bands are not available in L8 imagery and SWIR wavelength region is not available for PS imagery.

### 2.5. Grasslands FVC spectral signature analysis

To have a first understanding of the spectral signature of grasslands with various FVC, plots were grouped based on their reference FVC in six categories. The first category contains bare soils with no vegetational cover, the other five categories gather the plots based on their FVC from 1 to 100% FVC with a step of 20%. Then, for each imagery and for each band we built a boxplot graphical representation of the reflectances, grouped according to their FVC category. FVC categories were used only to display FVC levels in Figs. 2 and 3 and not to define the classes for a classification predictive model. Instead, FVC prediction was performed through Fractional Response Models, as described in the following paragraph.

**Table 1**
Description of vegetation indices evaluated in this study[1].

| Index name | Formula | L8 bands | S2 bands | PS bands | Reference |
|---|---|---|---|---|---|
| EVI[2] (Enhanced Vegetation Index) | $G^{*}\frac{NIR - RED}{(NIR + C_1RED - C_2BLUE) + L}$ | 2,4,5 | 2,4,8 | 2,6,8 | (Huete et al., 2002) |
| GNDVI (Green Normalized Difference Vegetation Index) | $\frac{NIR - GREEN}{NIR + GREEN}$ | 3,5 | 3, 8A | 4,8 | (Gitelson et al., 1996) |
| GVMI (Global Vegetation Moisture Index) | $\frac{(NIR + 0.1) - (SWIR + 0.02)}{(NIR + 0.1) + (SWIR + 0.02)}$ | 5,7 | 8,12 | – | (Ceccato et al., 2002) |
| MSAVI (Modified Soil Adjusted Vegetation Index) | $0.5^{*}(2NIR + 1 - \sqrt{(2^{*}NIR + 1)^2 - 8(NIR - RED)})$ | 4,5 | 4,8 | 6,8 | (Qi et al., 1994) |
| NBR (Normalized Burn Ratio) | $\frac{NIR - SWIR}{NIR + SWIR}$ | 5,7 | 8A,12 | – | (García & Caselles, 1991) |
| NDGI (Normalized Difference Greenness Index) | $\frac{GREEN - RED}{GREEN + RED}$ | 3,4 | 3,4 | 4,6 | (Courel et al., 1991) |
| NDMI (Normalized Difference Moisture Index) | $\frac{NIR - SWIR}{NIR + SWIR}$ | 5,6 | – | – | (Hardisky et al., 1983) |
| NDII (Normalized Difference Infrared Index) | $\frac{NIR - SWIR}{NIR + SWIR}$ | – | 8,11 | – | (Hardisky et al., 1983) |
| NDRE1 (Normalized Difference RE1) | $\frac{REDEDGE_{740} - REDEDGE_{705}}{REDEDGE_{740} + REDEDGE_{705}}$ | – | 5,6 | – | (Gitelson & Merzlyak, 1994) |
| NDVI (Normalized Difference Vegetation Index) | $\frac{NIR - RED}{NIR + RED}$ | 4,5 | 4,8 | 6,8 | (Rouse et al., 1974) |
| PSRI (Plant Senescence Reflectance Index) | $\frac{RED - BLUE}{REDEDGE_{705}}$ | – | 2,4,5 | 2,6,7 | (Merzlyak et al., 1999) |
| RECI (Red- Edge Chlorophyll Index) | $\left(\frac{NIR}{REDEDGE_{705}}\right) - 1$ | – | 5,8A | 7,8 | (Gitelson et al., 2003) |
| RENDVI (Red-Edge Normalized Difference Vegetation Index) | $\frac{NIR - REDEDGE_{705}}{NIR + REDEDGE_{705}}$ | – | 5,8A | 7,8 | (Gitelson & Merzlyak, 1994) |
| RESI (Red-Edge Spectral indices) | $\frac{REDEDGE_{780} + REDEDGE_{740} - REDEDGE_{705}}{REDEDGE_{780} + REDEDGE_{740} + REDEDGE_{705}}$ | | 5,6,7 | | (Xiao et al., 2020) |
| RVI (Ratio Vegetation Index) | $NIR/RED$ | 4,5 | 4,8 | 6,8 | (Jordan, 1969) |
| SAVI[3] (Soil adjusted Vegetation Index) | $\frac{NIR - RED}{NIR + RED + L}^{*}(1 + L)$ | 4,5 | 4,8 | 6,8 | (Huete, 1988) |
| VARI (Visible Atmospherically Resistant Index) | $\frac{GREEN - RED}{GREEN + RED - BLUE}$ | 2,3,4 | 2,3,4 | 2,4,6 | (Gitelson, 2001) |
| WDRVI (Wide Dynamic Range Vegetation Index | $\frac{0.1^{*}NIR - RED}{0.1^{*}NIR + RED}$ | 4,5 | 4,8A | 6,8 | (Gitelson, 2004) |

[1] NIR indicates near infrared; RED, red band; BLUE, blue band; GREEN, green band; SWIR, shortwave infrared band; REDEDGE, red-edge band.
[2] G indicates Gain factor, was set to 2.5; $C_1$ and $C_2$ are coefficients of the aerosol resistance term, were set to 6 and 7.5, respectively; L indicates canopy background adjustment, was set to 1.
[3] L indicates soil brightness correction factor, was set to 0.5.

### 2.6. Relationship between fractional vegetation cover and vegetation indices

First, for each imagery and for each VI we explored the indices variability inside and among FVC categories. Since the dependent variable (FVC) has a fractional nature, being bounded in the unit interval, the relationships between VIs and FVC were examined through Fractional Response Models using the *frm* function of the *frm* R package (Ramalho, 2019) (see Fig. S2 for the workflow diagram). We used *logit* as a link function and quasi-likelihood method to determine parameters (eq.2). The standard fractional regression model used is defined by the following conditional expectation:

$$E(y_i|x_i) = \frac{e^{x_i\theta}}{1 - e^{x_i\theta}} \quad (2)$$

where $y_i$ denote the fractional response variable, defined on the interval [0,1], to be explained for individual $i$, $i = 1, \ldots, N$. $x_i$ denote the explanatory variable and $\theta$ the vector of parameters of interest. R-squared ($R^2$), calculated as the square of the correlation coefficient between the actual and fitted values of the dependent variable, was used for model comparison. Selected models' residuals were checked for normality and homoscedasticity by visual inspection of the residuals plot.

The residuals of the selected models were regressed against all the other indices to find eventual promising predictors for multiple VIs models. To identify possible causes of error, we tested if there were correlations between selected models' residuals and some terrain indices that may affect plot spectral signature. Altitude, aspect, slope, topographic position index (TPI), terrain ruggedness index (TRI) and roughness were computed using the *terrain* function of the *raster* package in R. The terrain indices were computed according to Wilson et al. (2007). TRI is the mean of the absolute differences between the altitude value of a cell and the value of its eight surrounding cells. TPI is the difference between the altitude value of a cell and the mean value of its eight surrounding cells. Roughness is the difference between the maximum and the minimum value of a cell and its eight surrounding cells. To derive the terrain indices, we used a digital terrain model distributed by the Provincia Autonoma di Trento (PAT, 2016) with 10 m spatial resolution. Correlations were tested using the *cor.test* function in R, which tests for association between paired samples, using Pearson's product moment correlation coefficient (level of significance p-value $<$ 0.05). We also tested if within plot FVC heterogeneity (standard deviation of FVC across subplots) was correlated to the residuals.

### 2.7. Model validation

Cross validated statistics ($R^2_{CV}$) with leave-one-out procedure were computed to estimate the generalization capability of the selected models. The selected models for the L8, S2 and PS imagery were applied to estimate the FVC of all the grasslands of the study site and maps were analysed. The models were also applied on consecutive clear-sky images from summer 2021 to autumn 2021 on an area of recent grassland revegetation. The estimated FVC maps were plotted and compared to RGB visualization to assess if they show coherent spatial and temporal patterns.

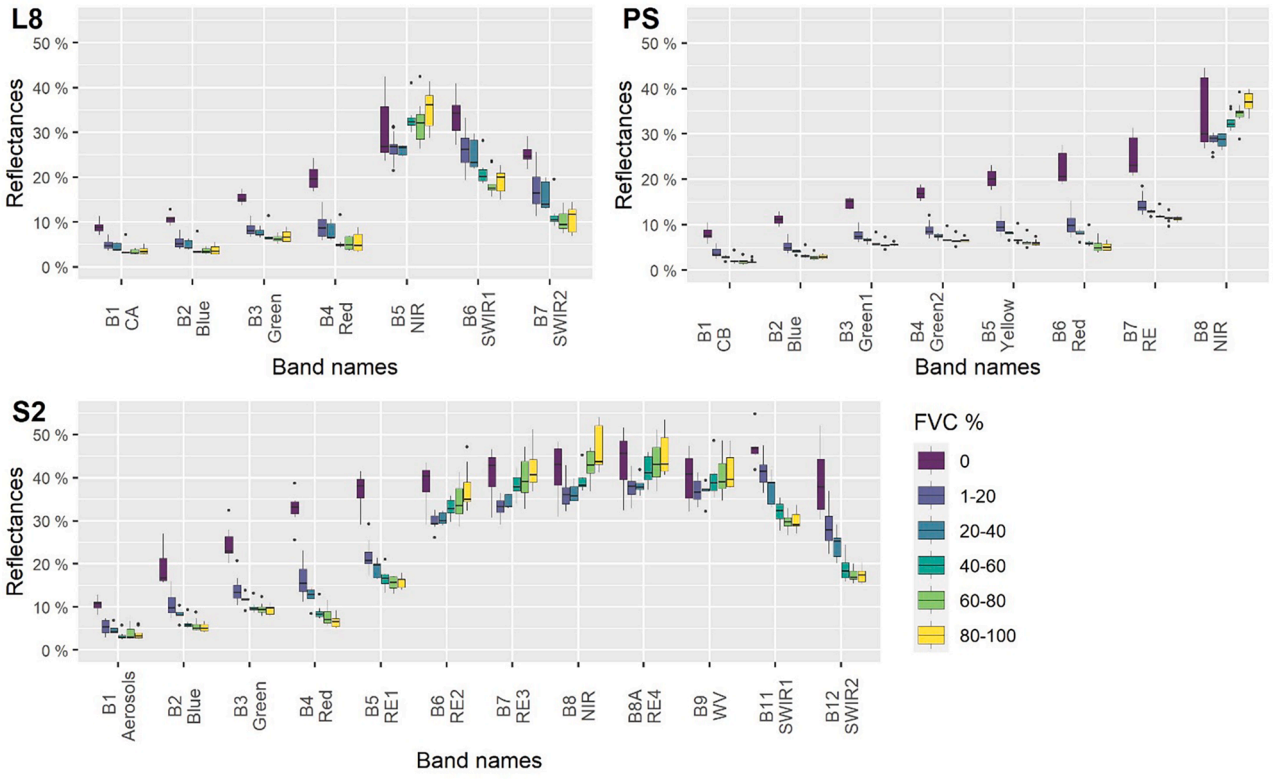


**Fig. 2.** Boxplot of the spectral values of the plots divided according to FVC% using L8, S2 and PS imagery. See Table S1 for band names abbreviations.

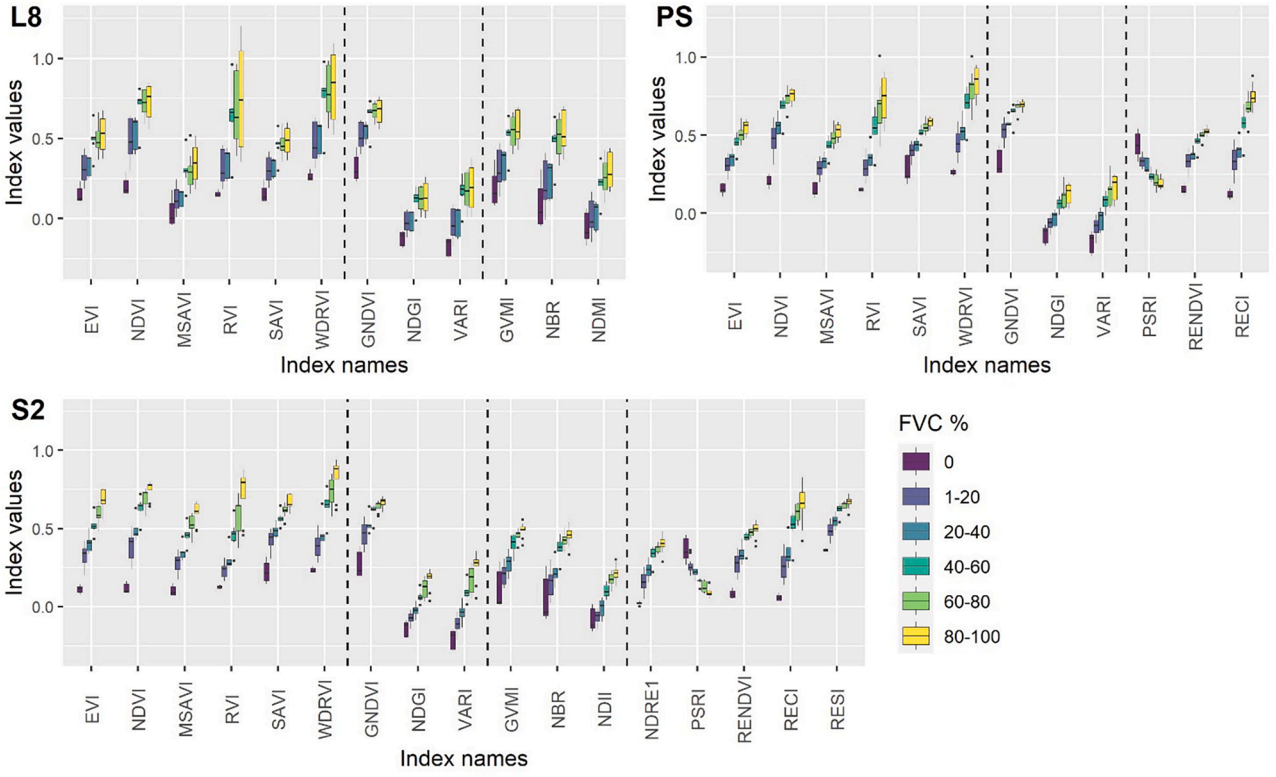


**Fig. 3.** Vegetation indices values of plots with various FVC. From left to right VIs based on NIR and red wavelength regions (EVI, NDVI, MSAVI, RVI, SAVI, WDRVI), including the green wavelength region (GNDVI, NDGI, VARI), based on SWIR and NIR wavelength regions (GVMI, NBR, NDII, NDMI) and indices based on Red Edge wavelengths (NDRE1, PSRI, RENDVI, RECI, RESI) were presented. RECI values were divided by 10, RENDVI by 3 and 1 was added to WDRVI to fit the figure y axis.

## 3. Results

### 3.1. Grasslands FVC spectral signature

Grasslands spectral signature is clearly affected by FVC level and there is great consistency between different satellites (Fig. 2). There is a linear relationship between FVC and reflectance values in the visible and SWIR domain. On the contrary, the NIR wavelength region (~865 nm: SR_B5, B8, b8) and the S2 Red-Edge2 and Red-Edge3 bands (B6 and B7) do not show a linear relationship with FVC along all the FVC gradient: reflectances show a positive correlation with FVC in vegetated plots, but bare soil plots have higher reflectance values and show a much higher variability. The SWIR bands are available only on L8 and S2 imagery (~1610 nm: SR_B6, B11) and are quite informative for low FVC, but tend to saturate at high FVC levels, similarly to red bands imagery (~665 nm: B4, b6).

### 3.2. Relationship between fractional vegetation cover and vegetation indices

VIs provided a higher separability of FVC categories than bands' reflectances. In addition, VIs relationship with FVC was coherent on the whole FVC gradient, whereas bare soils showed a different pattern from vegetated areas looking at bands' reflectances. The spectral separability of the FVC categories varies among different VIs and imageries, as presented in Fig. 3. Indices based on NIR and red wavelength regions (EVI, NDVI, MSAVI, RVI, SAVI, WDRVI) and on the visible wavelength region (GNDVI, NDGI, VARI) showed a clear relationship to FVC values. Indices based on SWIR and NIR wavelength regions (GVMI, NBR, NDII, NDMI) showed overlapping index values for low FVC levels, whereas indices based on red-edge wavelengths showed a promising identification of bare soils and low-density grassland but tends to saturate at higher FVC (NDRE1, PSRI, RENDVI, RECI, RESI).

In Table 2 the accuracy of FVC prediction models based on VI are presented. VIs derived from S2 and PS imagery showed a higher prediction ability than those based on L8 imagery. The best performing index for S2 imagery was EVI, which showed a strong relationship with FVC ($R^2 = 0.91$). The best performing index using PS imagery was RECI ($R^2 = 0.89$), whereas NDMI gave the highest correlation using L8 imagery ($R^2 = 0.66$) (Fig. 4). L8 model residuals showed a high degree of heteroscedasticity, whereas S2 and PS models residuals were almost homoscedastic (Fig. 4). The residuals of the selected models were regressed against all the other indices and some significant linear or quadratic relationships were found. The addition of a second VI to the selected model, however, led to a very low (<0.01) increase in $R^2$. No multiple VI models were therefore selected.

Terrain indices and diversity of FVC across subplots of each plot do not significantly explain the variability of the residuals, as resulting from Pearson's product moment correlation coefficient analysis (level of significance p-value < 0.05).

**Table 2**
Accuracy ($R^2$) of Fractional Response Models. The best model for each imagery is highlighted in green.

| Index | Spectral region of interest | Landsat-8 | Sentinel-2 | PlanetScope |
|---|---|---|---|---|
| EVI | NIR and Red included | 0.585 | 0.911 | 0.881 |
| NDVI | | 0.556 | 0.878 | 0.844 |
| MSAVI | | 0.558 | 0.893 | 0.875 |
| RVI | | 0.506 | 0.839 | 0.822 |
| SAVI | | 0.589 | 0.896 | 0.881 |
| WDRVI | | 0.536 | 0.840 | 0.839 |
| GNDVI | Green included | 0.564 | 0.794 | 0.823 |
| NDGI | | 0.516 | 0.864 | 0.813 |
| VARI | | 0.517 | 0.870 | 0.821 |
| GVMI | SWIR, NIR | 0.606 | 0.869 | – |
| NBR | | 0.605 | 0.819 | – |
| NDII | | – | 0.902 | – |
| NDMI | | 0.659 | – | – |
| NDRE1 | Red-Edge included | – | 0.851 | – |
| PSRI | | – | 0.895 | 0.805 |
| RENDVI | | – | 0.823 | 0.893 |
| RECI | | – | 0.821 | 0.895 |
| RESI | | – | 0.852 | – |

### 3.3. Model validation

The relationship between EVI derived from S2 imagery and FVC resulted in an $R^2$ of 0.911 and in a 0.903 cross validation $R^2$, whereas the $R^2$ and cross-validation $R^2$ for L8 were 0.659 and 0.636 respectively, and 0.895 and 0.886 for PS.

RGB visualization and FVC maps derived from selected S2 and PS models showed coherent spatial patterns, whereas some anomalous values were found in the map derived from the selected L8 model (Fig. 5). In the western and northern areas, the map derived from L8 imagery showed estimated values around 20% FVC, even though the RGB visualization and the estimated map derived from S2 and PS imagery showed bare soils or very low FVC. In addition to this, the great spatial heterogeneity of FVC in the study site is adequately described by S2 and PS spatial resolution, whereas the spatial resolution of L8 imagery (30 m) is not sufficient: in many L8 pixels low- and high-density grasslands are mixed, and forest mixed pixels may occur.

In the temporal change analysis FVC maps derived from S2 and PS imagery showed coherent patterns to RGB visualization and accurately described grassland recovery after soil levelling and sowing for ski runs preparation (Fig. 6). The FVC maps derived from L8 overestimated the grassland cover at the beginning of the season compared to RGB visualization and to maps derived from S2 and PS imageries.

## 4. Discussion

### 4.1. Spectral signatures, VIs and their relationship with FVC

Soil and plant spectral signature identification and discrimination may not be straightforward using raw spectral band reflectances, but VIs may accentuate the spectral distinctness. The understanding of soil and plant spectral features is fundamental for FVC prediction, but there is not always a clear linear relationship between reflectances and FVC on the whole FVC gradient. While in vegetated plots FVC seems to play a major role, the spectral signature of bare plots is much more variable and has been attributed to the combined effect of their origin, parental material, structure, mineralogy, water content and organic matter content (Fabre et al., 2015; Lausch et al., 2019; Mulder et al., 2011; Wilson et al., 2017; Xu et al., 2020). In our case study, we observed that the spectral signature changes along the FVC gradient following specific patterns. In the first stages of the revegetation process the high reflectance value of bare soils in the visible and NIR wavelength regions decrease, probably due to plant shadowing effect and plant spectral signature, and partly due to the increase of soil organic matter content and soil water-holding capacity (Bartholomeus et al., 2008; Fabre et al., 2015). In the later stages of the revegetation plants spectral signature plays a major role and soils diversity is almost hidden. At high FVC levels, reflectances in the blue (450 nm) and red (670 nm) regions further strongly decrease due to high plant chlorophyll absorption resulting in higher reflectances than in low covered areas (Govender et al., 2009).

Since raw bands values do not always allow spectral distinctness, researchers identified several band differences and ratios that were found to accentuate spectral distinctness and developed VIs based on these findings (Xue and Su, 2017). One common observation is that the difference between NIR and red reflectance for soil is much less than for live vegetation (Huete, 1988; Rouse et al., 1974). In our case study VIs based on the difference between NIR and red wavelength regions (EVI, NDVI, MSAVI, RVI, SAVI, WDRVI) confirmed their high correlation to FVC and their robustness in the correct identification of bare soils, as

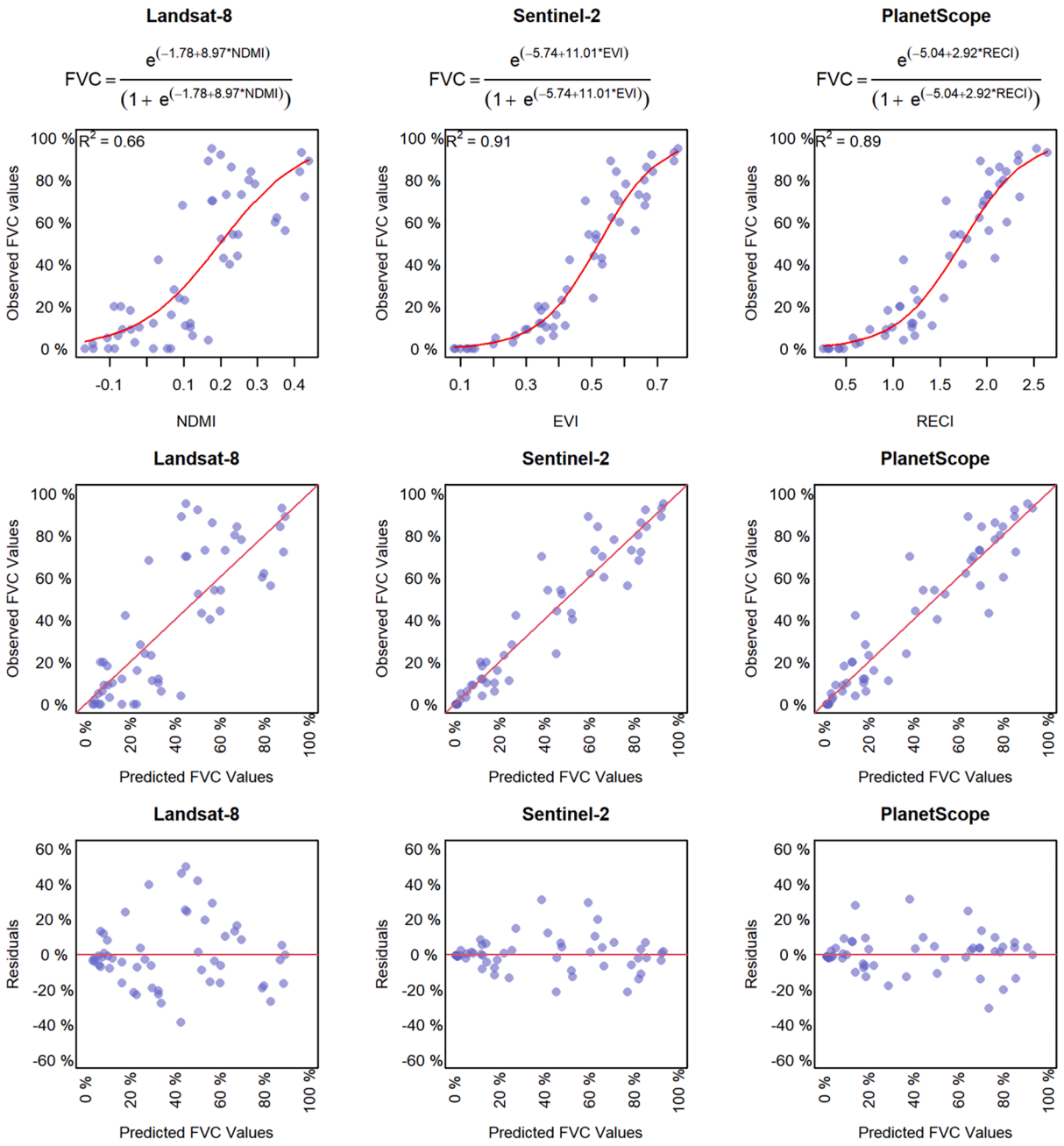


**Fig. 4.** Reference FVC values plotted against values estimated using selected prediction models derived from Landsat-8, Sentinel-2 and PlanetScope imagery and against models' residuals.

reported in previous literature (Chen et al., 2016; Jia et al., 2017; Kim et al., 2020; Mao et al., 2022). EVI was selected as the best performing index for S2 imagery. VARI and NDGI, that are based on the visible spectral domain, were used just twice for FVC estimation (Jiménez-Muñoz et al., 2009; Zhou et al., 2014) and in our case study showed a strong relationship with FVC ($R^2 = 0.864$ for NDGI, and 0.870 for VARI using S2 imagery). The good performance of these indices is promising since the visible domain is the most common wavelength region and may benefit from future further improvements of spatial and temporal resolution (Dubovik et al., 2021; Garzaniti et al., 2021). The red-edge spectral bands are available only for S2 and PS imagery and the derived indices tested (NDRE1, PSRI, RENDVI, RECI and RESI) have been indicated as promising by previous literature (Gao et al., 2020; Gitelson, 2013; Liu et al., 2007). In our case study these indices showed very good performances. Even though they tend to saturate in very dense grasslands, we obtained high accuracies and RECI was selected as the best performing index for PS imagery. Indices based on SWIR and NIR wavelength regions (GVMI, NBR, NDII, NDMI) are typically used for the analysis of vegetation moisture content, but NDII was found to be strictly correlated to FVC as it outperformed other indices in a mowing detection algorithm (Andreatta et al., 2022). In our case study, however, only using L8 imagery the relationship between NDMI and FVC resulted in the highest $R^2$, but the model showed heteroscedasticity in the residuals (Fig. 4) and performed badly at the spatial change analysis (Fig. 5, see subsection 4.2 for discussion).

The observed heteroscedasticity of L8 model residuals is caused by high residual standard deviation for FVC predicted values in the mid-range. Three plots which showed very high positive residuals (plot 18, 32 and 4) have high reference FVC, but they are contiguous to areas with very low vegetation cover. The mixed spectral signature of the pixel in

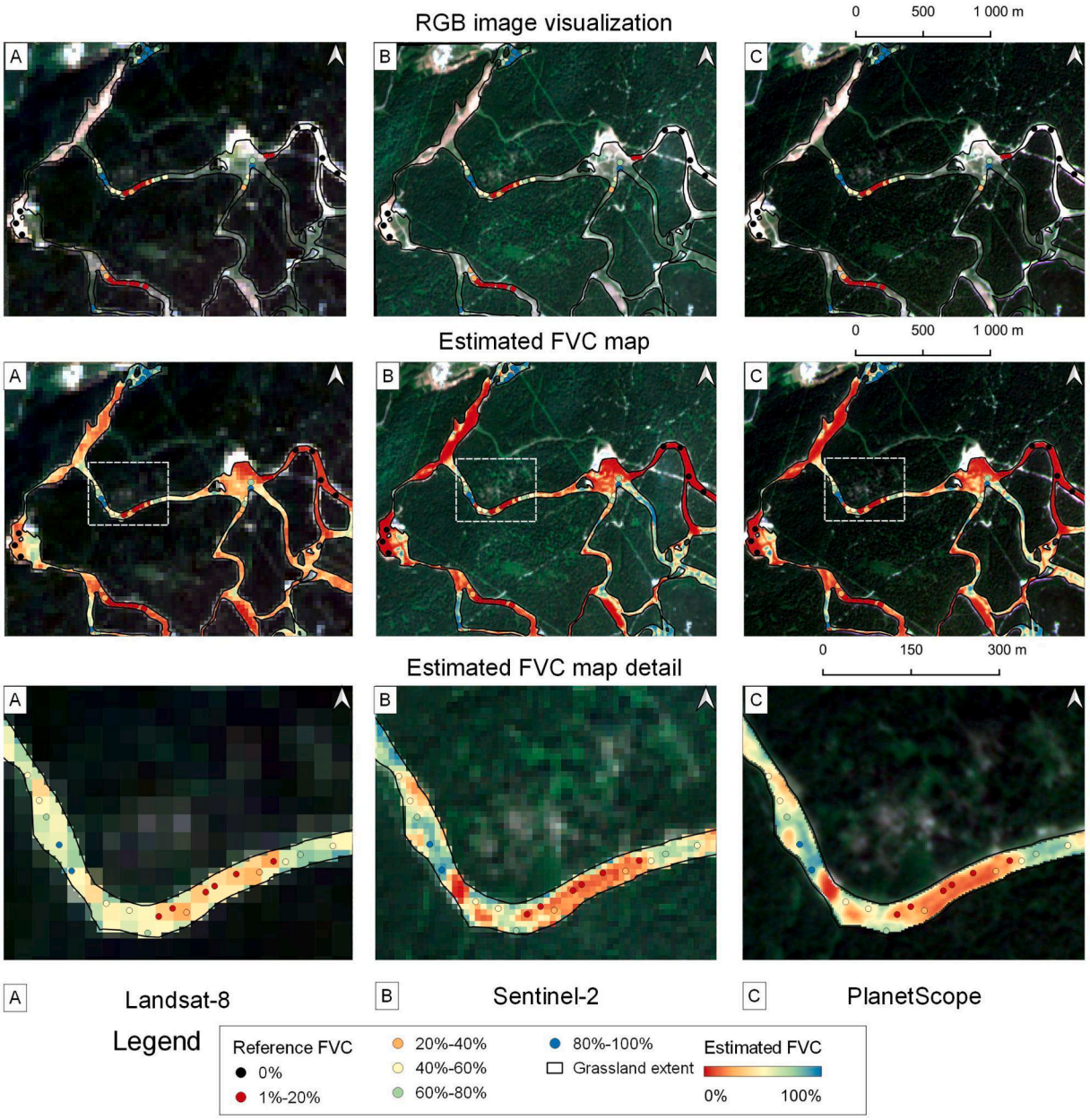


**Fig. 5.** FVC spatial change analysis. RGB imagery, estimated FVC map and estimated FVC map detail obtained using the best prediction model based on L8, S2, and PS imagery.

which these plots are located results in an estimated FVC in the mid-range. The opposite happens for plots 36, 37, 39, 40 and 41 which show large negative residuals, as the plots are scarcely vegetated, but inside their pixels there are areas covered by bushes and small trees. The mixed spectral signature also in this case results in an estimated FVC in the mid-range, but in large negative residuals. The absence of large residuals for low and high estimated FVC may be explained: their NDMI values are coherent with values attributed to plots located in pure pixels. On the contrary, NDMI values in the mid-range in some cases result as an average of high and low FVC areas inside the pixels. The absence of any significant relationship between residuals of L8 model and variability of FVC across subplots of each plot can be related to L8 imagery resolution: even though some L8 pixels (30 m × 30 m) included heterogeneous vegetations (high model residuals), the plots used to describe them in the field (10 m × 10 m) were vegetationally homogeneous (low standard deviation of FVC across subplot).

In our case study the addition of a second VI to the FVC prediction model did not increase the accuracy (increase in $R^2 < 0.01$) and was therefore not applied. The addition of several indices to FVC prediction models is not common, but has been explored, for example by Guerschman et al. (2009).

### 4.2. Model validation

Cross validated statistics and spatiotemporal change analysis of FVC assessed the good generalization capability of the selected S2 and PS models but raised some concerns regarding the L8 model. Cross validated statistics were just slightly lower than accuracy metrics obtained on the whole calibration dataset (Table S2), and the estimated FVC derived from S2 and PS imagery maps and RGB visualization showed coherent spatial patterns. Two factors related to the spatial resolution of the L8 imagery probably affected the L8 model reliability. Firstly, the calibration plot size (10 m × 10 m) was not sufficient to describe the vegetation of the whole L8 pixel, so a not representative reference FVC is

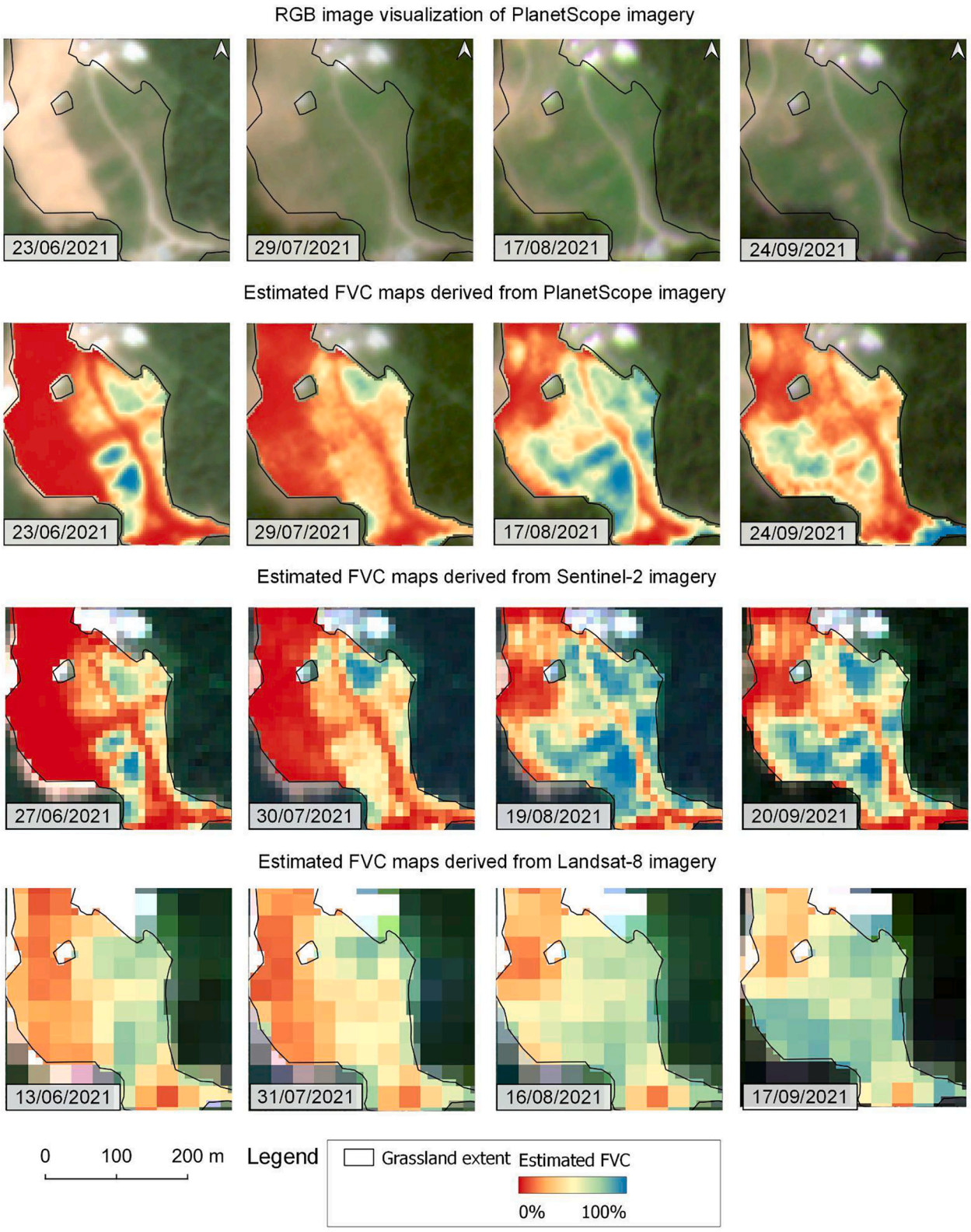


**Fig. 6.** FVC temporal change analysis. RGB visualization (PS imagery) and estimated FVC map computed using best PS, S2 and L8 prediction models for 4 consequent clear-sky images of grasslands recovering after soil levelling and sowing for ski runs preparation.

assigned to mixed pixels. The L8 model is therefore trained with misleading data, resulting in a heteroscedastic distribution of the residuals, in erroneous prediction of the bare soil areas in the west and north areas of the study site (Fig. 5) and in an overestimation of the frequency of FVC values in the mid-range (Fig. 4). Secondly, in our study site FVC changes at a very fine spatial scale, so that the coarser spatial resolution of L8 imagery (30 m) is not sufficient at describing it, and even if 30 m × 30 m reference FVC was available, locally extreme FVC would be averaged at pixel scale. While L8 model performance was not satisfying, as already discussed, S2 and PS imagery provided coherent

results and especially PS imagery derived FVC maps provided a much finer description of FVC distribution in space.

The temporal change analysis was used to assess the reliability of the selected models when applied on different images and confirmed their robustness.

## 5. Conclusions

In this study we assessed that S2 and PS imagery can successfully be used to estimate grassland FVC in areas where it changes at a very fine scale, thanks to their high spatial resolution and to the availability of the red-edge wavelength region. Previously available imagery at medium to low spatial and temporal resolution (e.g. L8) may still be interesting for analysis requiring long time-series, since long-term FVC data is a useful indicator of land degradation and recovery processes, especially for vast agricultural and natural grasslands. However, for local hotspots of degradation and recovery, high-resolution FVC estimated from S2 and PS imagery would be useful to examine the spatial and temporal patterns patches better than the mid- or coarse-resolution satellite data. The selected models should be carefully applied to areas different from the study site since soil reflectance depends on multiple factors and significantly affects the pixel spectral signature in areas with low FVC.

*CRediT authorship contribution statement*

**Davide Andreatta:** Conceptualization, Formal analysis, Investigation, Software, Writing – original draft, Writing – review & editing. **Damiano Gianelle:** Conceptualization, Resources, Funding acquisition, Writing – review & editing, Supervision. **Michele Scotton:** Conceptualization, Resources, Funding acquisition, Writing – review & editing, Supervision. **Michele Dalponte:** Conceptualization, Software, Writing – review & editing, Supervision.

## Declaration of Competing Interest

The authors declare that they have no known competing financial interests or personal relationships that could have appeared to influence the work reported in this paper.

## Data availability

Field fractional vegetation cover data and location are provided in KML format as supplementary materials, imageries can be accessed through the Planet website (https://www.planet.com) and through the Earth Engine Data Catalog (https://developers.google.com/earth-engine/datasets).

## Acknowledgements

The authors would like to thank Planet Labs, Inc. for providing access to their daily imagery through the education and research program. This work was funded by the Highlander project co-financed by the Connecting European Facility Programme of the European Union Grant agreement n° INEA/CEF/ICT/A2018/1815462.

## Appendix A. Supplementary data

Supplementary data to this article can be found online at https://doi.org/10.1016/j.ecolind.2022.109102. These data include Google maps of the most important areas described in this article.

## References

Andreatta, D., Gianelle, D., Scotton, M., Vescovo, L., Dalponte, M., 2022. Detection of grassland mowing frequency using time series of vegetation indices from Sentinel-2 imagery. GIScience Remote Sens. 59 (1), 481–500. https://doi.org/10.1080/15481603.2022.2036055.

Atzberger, C., 2004. Object-based retrieval of biophysical canopy variables using artificial neural nets and radiative transfer models. Remote Sens. Environ. 93 (1–2), 53–67. https://doi.org/10.1016/J.RSE.2004.06.016.

Baret, F., Hagolle, O., Geiger, B., Bicheron, P., Miras, B., Huc, M., Berthelot, B., Niño, F., Weiss, M., Samain, O., Roujean, J.L., Leroy, M., 2007. LAI, fAPAR and fCover CYCLOPES global products derived from VEGETATION. Remote Sens. Environ. 110 (3), 275–286. https://doi.org/10.1016/j.rse.2007.02.018.

Bartholomeus, H.M., Schaepman, M.E., Kooistra, L., Stevens, A., Hoogmoed, W.B., Spaargaren, O.S.P., 2008. Spectral reflectance based indices for soil organic carbon quantification. Geoderma 145 (1–2), 28–36. https://doi.org/10.1016/j.geoderma.2008.01.010.

Booth, D.T., Cox, S.E., Berryman, R.D., 2006. Point sampling digital imagery with 'Samplepoint'. Environ. Monit. Assess. 123 (1–3), 97–108. https://doi.org/10.1007/s10661-005-9164-7.

Booth, T.D., Cox, S.E., Fifield, C., Phillips, M., Williamson, N., Booth, D.T., Cox, S.E., Fifield, C., Phillips, M., Willlamson, N., 2005. Image analysis compared with other methods for measuring ground cover. Arid Land Res. Manage. 19 (2), 91–100. https://doi.org/10.1080/15324980590916486.

Ceccato, P., Gobron, N., Flasse, S., Pinty, B., Tarantola, S., 2002. Designing a spectral index to estimate vegetation water content from remote sensing data: Part 1: Theoretical approach. Remote Sens. Environ. 82 (2-3), 188–197.

Chen, J., Yi, S., Qin, Y., Wang, X., 2016. Improving estimates of fractional vegetation cover based on UAV in alpine grassland on the Qinghai-Tibetan Plateau. Int. J. Remote Sens. 37 (8), 1922–1936. https://doi.org/10.1080/01431161.2016.1165884.

Courel, M.-F., Chamard, P., Guenegou, M., Lerhun, J., Levasseur, J., Togola, M., 1991. Utilisation des bandes spectrales du vert et du rouge pour une meilleure évaluation des formations végétales actives. Télédétection et Cartographie 203–209. https://hal.archives-ouvertes.fr/hal-00327879.

Darvishzadeh, R., Skidmore, A., Schlerf, M., Atzberger, C., 2008. Inversion of a radiative transfer model for estimating vegetation LAI and chlorophyll in a heterogeneous grassland. Remote Sens. Environ. 112 (5), 2592–2604. https://doi.org/10.1016/j.rse.2007.12.003.

Dubovik, O., Schuster, G.L., Xu, F., Hu, Y., Bösch, H., Landgraf, J., Li, Z., 2021. Grand challenges in satellite remote sensing. Front. Remote Sens. 2, 1. https://doi.org/10.3389/frsen.2021.619818.

Fabre, S., Briottet, X., Lesaignoux, A., 2015. Estimation of soil moisture content from the spectral reflectance of bare soils in the 0.4–2.5 μm domain. Sensors 15 (2), 3262–3281. https://doi.org/10.3390/s150203262.

Gang, C., Zhou, W., Chen, Y., Wang, Z., Sun, Z., Li, J., Qi, J., Odeh, I., 2014. Quantitative assessment of the contributions of climate change and human activities on global grassland degradation. Environ. Earth Sci. 72 (11), 4273–4282. https://doi.org/10.1007/S12665-014-3322-6/FIGURES/5.

Gao, L., Wang, X., Johnson, B.A., Tian, Q., Wang, Y., Verrelst, J., Mu, X., Gu, X., 2020. Remote sensing algorithms for estimation of fractional vegetation cover using pure vegetation index values: a review. ISPRS J. Photogramm. Remote Sens. 159, 364–377. https://doi.org/10.1016/j.isprsjprs.2019.11.018.

García, M.J.L., Caselles, V., 1991. Mapping burns and natural reforestation using thematic Mapper data. Geocarto International 6 (1), 31–37. https://doi.org/10.1080/10106049109354290.

Garzaniti, N., Tekic, Z., Kukolj, D., Golkar, A., 2021. Review of technology trends in new space missions using a patent analytics approach. Prog. Aerosp. Sci. 125, 100727 https://doi.org/10.1016/j.paerosci.2021.100727.

Gitelson, A.A., 2001. Non-destructive and remote sensing techniques for estimation of vegetation status. Papers in Natural Resources 273. https://digitalcommons.unl.edu/natrespapers.

Gitelson, A.A., 2004. Wide dynamic range vegetation index for remote quantification of biophysical characteristics of vegetation. J. Plant Physiol. 161 (2), 165–173. https://doi.org/10.1078/0176-1617-01176.

Gitelson, A.A., 2013. Remote estimation of crop fractional vegetation cover: the use of noise equivalent as an indicator of performance of vegetation indices. Int. J. Remote Sens. 34 (17), 6054–6066. https://doi.org/10.1080/01431161.2013.793868.

Gitelson, A.A., Gritz †, Y., Merzlyak, M.N., 2003. Relationships between leaf chlorophyll content and spectral reflectance and algorithms for non-destructive chlorophyll assessment in higher plant leaves. J. Plant Physiol. 160 (3), 271–282.

Gitelson, A.A., Kaufman, Y.J., Merzlyak, M.N., 1996. Use of a green channel in remote sensing of global vegetation from EOS-MODIS. Remote Sens. Environ. 58 (3), 289–298. https://doi.org/10.1016/S0034-4257(96)00072-7.

Gitelson, A., Merzlyak, M.N., 1994. Quantitative estimation of chlorophyll-a using reflectance spectra: experiments with autumn chestnut and maple leaves. J. Photochem. Photobiol., B 22 (3), 247–252. https://doi.org/10.1016/1011-1344(93)06963-4.

Gorelick, N., Hancher, M., Dixon, M., Ilyushchenko, S., Thau, D., Moore, R., 2017. Google Earth Engine: planetary-scale geospatial analysis for everyone. Remote Sens. Environ. 202, 18–27. https://doi.org/10.1016/j.rse.2017.06.031.

Govender, M., Chetty, K., Bulcock, H., 2009. A review of hyperspectral remote sensing and its application in vegetation and water resource studies. Water SA 33 (2), 145–151. https://doi.org/10.4314/wsa.v33i2.49049.

Graetz, R.D., Pech, R.P., Davis, A.W., 1988. The assessment and monitoring of sparsely vegetated rangelands using calibrated Landsat data. Int. J. Remote Sens. 9 (7), 1201–1222. https://doi.org/10.1080/01431168808954929.

Guerschman, J.P., Hill, M.J., Renzullo, L.J., Barrett, D.J., Marks, A.S., Botha, E.J., 2009. Estimating fractional cover of photosynthetic vegetation, non-photosynthetic vegetation and bare soil in the Australian tropical savanna region upscaling the EO-1 Hyperion and MODIS sensors. Remote Sens. Environ. 113 (5), 928–945. https://doi.org/10.1016/J.RSE.2009.01.006.

Hardisky, M., Klemas, V., Smart, M., 1983. The influence of soil salinity, growth form, and leaf moisture on the spectral radiance of Spartina alterniflora canopies. Photogramm. Eng. Remote Sens. 49, 77–83.
Hijmans, R.J., 2021. raster: Geographic Data Analysis and Modeling. https://cran.r-project.org/package=raster.
Huete, A., 1988. A soil-adjusted vegetation index (SAVI). Remote Sens. Environ. 25 (3), 295–309. https://doi.org/10.1016/0034-4257(88)90106-X.
Huete, A., Didan, K., Miura, T., Rodriguez, E., Gao, X., Ferreira, L., 2002. Overview of the radiometric and biophysical performance of the MODIS vegetation indices. Remote Sens. Environ. 83 (1–2), 195–213. https://doi.org/10.1016/S0034-4257(02)00096-2.
Jáuregui, J.M., Delbino, F.G., Brance Bonvini, M.I., Berhongaray, G., 2019. Determining yield of forage crops using the Canopeo mobile phone app. J. New Zealand Grasslands 81, 41–46. https://doi.org/10.33584/JNZG.2019.81.385.
Jia, K., Li, Y., Liang, S., Wei, X., Yao, Y., 2017. Combining estimation of green vegetation fraction in an arid region from Landsat 7 ETM+ data. Remote Sensing 9 (11), 1121. https://doi.org/10.3390/rs9111121.
Jiménez-Muñoz, J., Sobrino, J., Plaza, A., Guanter, L., Moreno, J., Martinez, P., 2009. Comparison between fractional vegetation cover retrievals from vegetation indices and spectral mixture analysis: case study of PROBA/CHRIS data over an agricultural area. Sensors 9 (2), 768–793. https://doi.org/10.3390/s90200768.
Jordan, C.F., 1969. Derivation of leaf-area index from quality of light on the forest floor. Ecology 50 (4), 663–666. https://doi.org/10.2307/1936256.
Kim, J., Kang, S., Seo, B., Narantsetseg, A., Han, Y., 2020. Estimating fractional green vegetation cover of Mongolian grasslands using digital camera images and MODIS satellite vegetation indices. GIScience Remote Sens. 57 (1), 49–59. https://doi.org/10.1080/15481603.2019.1662166.
Lausch, A., Baade, J., Bannehr, L., Borg, E., Bumberger, J., Chabrilliat, S., Dietrich, P., Gerighausen, H., Glässer, C., Hacker, J., Haase, D., Jagdhuber, T., Jany, S., Jung, A., Karnieli, A., Kraemer, R., Makki, M., Mielke, C., Möller, M., Mollenhauer, H., Montzka, C., Pause, M., Rogass, C., Rozenstein, O., Schmullius, C., Schrodt, F., Schrön, M., Schulz, K., Schütze, C., Schweitzer, C., Selsam, P., Skidmore, A., Spengler, D., Thiel, C., Truckenbrodt, S., Vohland, M., Wagner, R., Weber, U., Werban, U., Wollschläger, U., Zacharias, S., Schaepman, M., 2019. Linking remote sensing and geodiversity and their traits relevant to biodiversity—Part I: Soil characteristics. Remote Sensing 11 (20), 2356.
Li, T., Cui, L., Scotton, M., Dong, J., Xu, Z., Che, R., Tang, L.i., Cai, S., Wu, W., Andreatta, D., Wang, Y., Song, X., Hao, Y., Cui, X., 2022. Characteristics and trends of grassland degradation research. J. Soils Sediments 22 (7), 1901–1912.
Li, X.-B., Chen, Y.-H., Yang, H., Zhang, Y.-X., 2005. Improvement, comparison, and application of field measurement methods for grassland vegetation fractional coverage. J. Integr. Plant Biol. 47 (9), 1074–1083. https://doi.org/10.1111/j.1744-7909.2005.00134.x.
Liang, S., & Wang, J. (2020). Fractional vegetation cover. In Academic Press (Ed.), *Advanced Remote Sensing* (Second edi, pp. 477–510). Elsevier. doi: 10.1016/B978-0-12-815826-5.00012-X.
Liu, Z.-Y., Huang, J.-F., Wu, X.-H., Dong, Y.-P., 2007. Comparison of vegetation indices and red-edge parameters for estimating grassland cover from canopy reflectance data. J. Integr. Plant Biol. 49 (3), 299–306.
Lollato, R.P., Ochsner, T.E., Arnall, D.B., Griffin, T.W., Edwards, J.T., 2019. From field experiments to regional forecasts: upscaling wheat grain and forage yield response to acidic soils. Agron. J. 111 (1), 287–302. https://doi.org/10.2134/AGRONJ2018.03.0206.
Mao, P., Zhang, J., Li, M., Liu, Y., Wang, X., Yan, R., Shen, B., Zhang, X., Shen, J., Zhu, X., Xu, D., Xin, X., 2022. Spatial and temporal variations in fractional vegetation cover and its driving factors in the Hulun Lake region. Ecol. Ind. 135, 108490 https://doi.org/10.1016/J.ECOLIND.2021.108490.
McCallum, J. B., 2000. SigmaScan Pro 5.0. *Science*, *289*(5478), 412–412. https://go.gale.com/ps/i.do?p=HRCA&sw=w&issn=00368075&v=2.1&it=r&id=GALE%7CA63940621&sid=googleScholar&linkaccess=fulltext.
McGwire, K., Minor, T., Fenstermaker, L., 2000. Hyperspectral mixture modeling for quantifying sparse vegetation cover in arid environments. Remote Sens. Environ. 72 (3), 360–374. https://doi.org/10.1016/S0034-4257(99)00112-1.
Merzlyak, M.N., Gitelson, A.A., Chivkunova, O.B., Rakitin, V.Y., 1999. Non-destructive optical detection of pigment changes during leaf senescence and fruit ripening. Physiol. Plant. 106 (1), 135–141. https://doi.org/10.1034/J.1399-3054.1999.106119.X.
Mulder, V.L., de Bruin, S., Schaepman, M.E., Mayr, T.R., 2011. The use of remote sensing in soil and terrain mapping – a review. Geoderma 162 (1–2), 1–19. https://doi.org/10.1016/j.geoderma.2010.12.018.
PAT. (2016). Digital terrain model for hydrological applications. Provincia Autonoma di Trento. https://siat.provincia.tn.it/geonetwork/srv/ita/catalog.search;jsessionid=2FC489233B879F0A43023ECDAAFF5286#/metadata/p_TN:d6472d5e-94b7-456e-b633-0bf19daf6cdf.
Patrignani, A., Ochsner, T.E., 2015. Canopeo: a powerful new tool for measuring fractional green canopy cover. Agron. J. 107 (6), 2312–2320. https://doi.org/10.2134/agronj15.0150.
Qi, J., Chehbouni, A., Huete, A.R., Kerr, Y.H., Sorooshian, S., 1994. A modified soil adjusted vegetation index. Remote Sens. Environ. 48 (2), 119–126. https://doi.org/10.1016/0034-4257(94)90134-1.
Ramalho, J. J. S., 2019. Modeling fractional responses using R (pp. 245–279). doi: 10.1016/bs.host.2018.11.008.
Reynolds, S., Frame, J., 2005. Grasslands: Developments, Opportunities, Perspectives. Publishers, Science.
Roujean, J.L., Lacaze, R., 2002. Global mapping of vegetation parameters from POLDER multiangular measurements for studies of surface-atmosphere interactions: a pragmatic method and its validation. J. Geophys. Res.: Atmos. 107 (D12), ACL-6. https://doi.org/10.1029/2001JD000751.
Rouse, J.W., Haas, R., Schell, J., Deering, D., 1974. Monitoring vegetation systems in the Great Plains with ERTS. NASA Special Publication 351 (1974), 309.
RStudio Team. (2020). RStudio: Integrated Development Environment for R. http://www.rstudio.com/.
Sboarina, C., & Cescatti, A. (2004). Il clima del Trentino–distribuzione spaziale delle principali variabili climatiche Report 33. https://www.fmach.it/Servizi-Generali/Editoria/Il-clima-del-Trentino-distribuzione-spaziale-delle-principali-variabili-climatiche.
van der Meer, F., 1999. Image classification through spectral unmixing. In: Spatial Statistics for Remote Sensing. Springer, pp. 185–193.
Verrelst, J., Muñoz, J., Alonso, L., Delegido, J., Rivera, J.P., Camps-Valls, G., Moreno, J., 2012. Machine learning regression algorithms for biophysical parameter retrieval: Opportunities for Sentinel-2 and -3. Remote Sens. Environ. 118, 127–139. https://doi.org/10.1016/j.rse.2011.11.002.
Wang, B., Waters, C., Orgill, S., Cowie, A., Clark, A., Li Liu, D., Simpson, M., McGowen, I., Sides, T., 2018. Estimating soil organic carbon stocks using different modelling techniques in the semi-arid rangelands of eastern Australia. Ecol. Ind. 88, 425–438. https://doi.org/10.1016/J.ECOLIND.2018.01.049.
White, M.A., Asner, G.P., Nemani, R.R., Privette, J.L., Running, S.W., 2000. Measuring fractional cover and leaf area index in arid ecosystems: digital camera, radiation transmittance, and laser altimetry methods. Remote Sens. Environ. 74 (1), 45–57. https://doi.org/10.1016/S0034-4257(00)00119-X.
Wilson, C.H., Caughlin, T.T., Rifai, S.W., Boughton, E.H., Mack, M.C., Flory, A.S.L., 2017. Multi-decadal time series of remotely sensed vegetation improves prediction of soil carbon in a subtropical grassland. Ecol. Appl. 27 (5), 1646–1656. http://www.jstor.org/stable/26294514.
Wilson, M.F.J., O'Connell, B., Brown, C., Guinan, J.C., Grehan, A.J., 2007. Multiscale terrain analysis of multibeam bathymetry data for habitat mapping on the continental slope. Mar. Geod. 30 (1–2), 3–35. https://doi.org/10.1080/01490410701295962.
Xiao, C., Li, P., Feng, Z., Liu, Y., Zhang, X., 2020. Sentinel-2 red-edge spectral indices (RESI) suitability for mapping rubber boom in Luang Namtha Province, northern Lao PDR. Int. J. Appl. Earth Obs. Geoinf. 93, 102176 https://doi.org/10.1016/J.JAG.2020.102176.
Xu, C., Qu, J.J., Hao, X., Wu, D., 2020. Monitoring surface soil moisture content over the vegetated area by integrating optical and SAR satellite observations in the permafrost region of Tibetan Plateau. Remote Sensing 12 (1). https://doi.org/10.3390/RS12010183.
Xue, J., Su, B., 2017. Significant remote sensing vegetation indices: a review of developments and applications. J. Sensors 2017, 1–17.
Zarei, A., Asadi, E., Ebrahimi, A., Jafari, M., Malekian, A., Mohammadi Nasrabadi, H., Chemura, A., Maskell, G., 2020. Prediction of future grassland vegetation cover fluctuation under climate change scenarios. Ecol. Ind. 119, 106858. https://linkinghub.elsevier.com/retrieve/pii/S1470160X20307962.
Zhou, Q., Robson, M., Pilesjo, P., 1998. On the ground estimation of vegetation cover in Australian rangelands. Int. J. Remote Sens. 19 (9), 1815–1820. https://doi.org/10.1080/014311698215261.
Zhou, Y., Zhang, L., Xiao, J., Chen, S., Kato, T., Zhou, G., 2014. A comparison of satellite-derived vegetation indices for approximating gross primary productivity of grasslands. Rangeland Ecol. Manage. 67, 9–18. https://doi.org/10.2111/REM-D-13-00059.1.

# SUPPLEMENTARY MATERIALS

Of the article ECOLIND-23053 “Estimating grassland vegetation cover with remote sensing: a comparison between Landsat-8, Sentinel-2 and PlanetScope imagery”

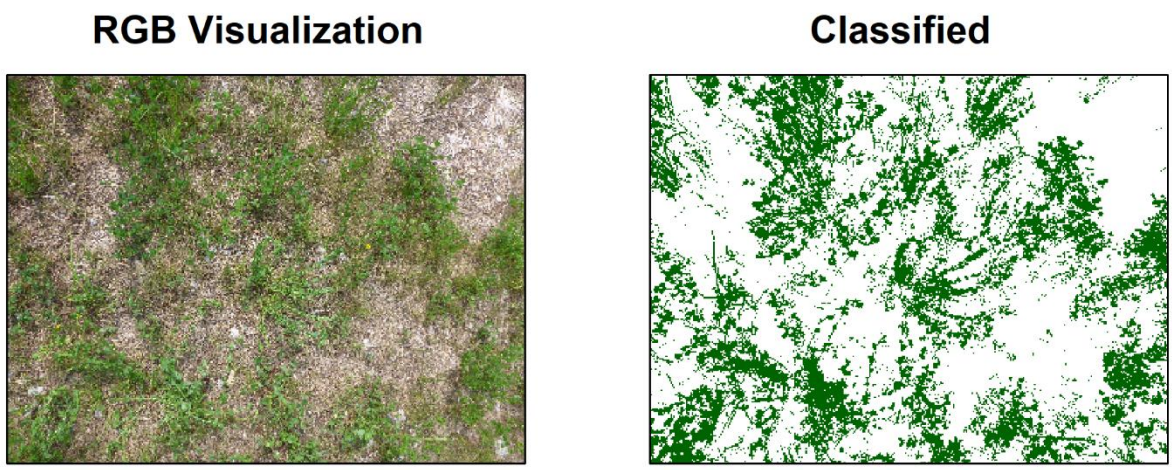


*Figure S1. Grassland subplot in RGB visualization and classified subplot (vegetation in green, other in white).*

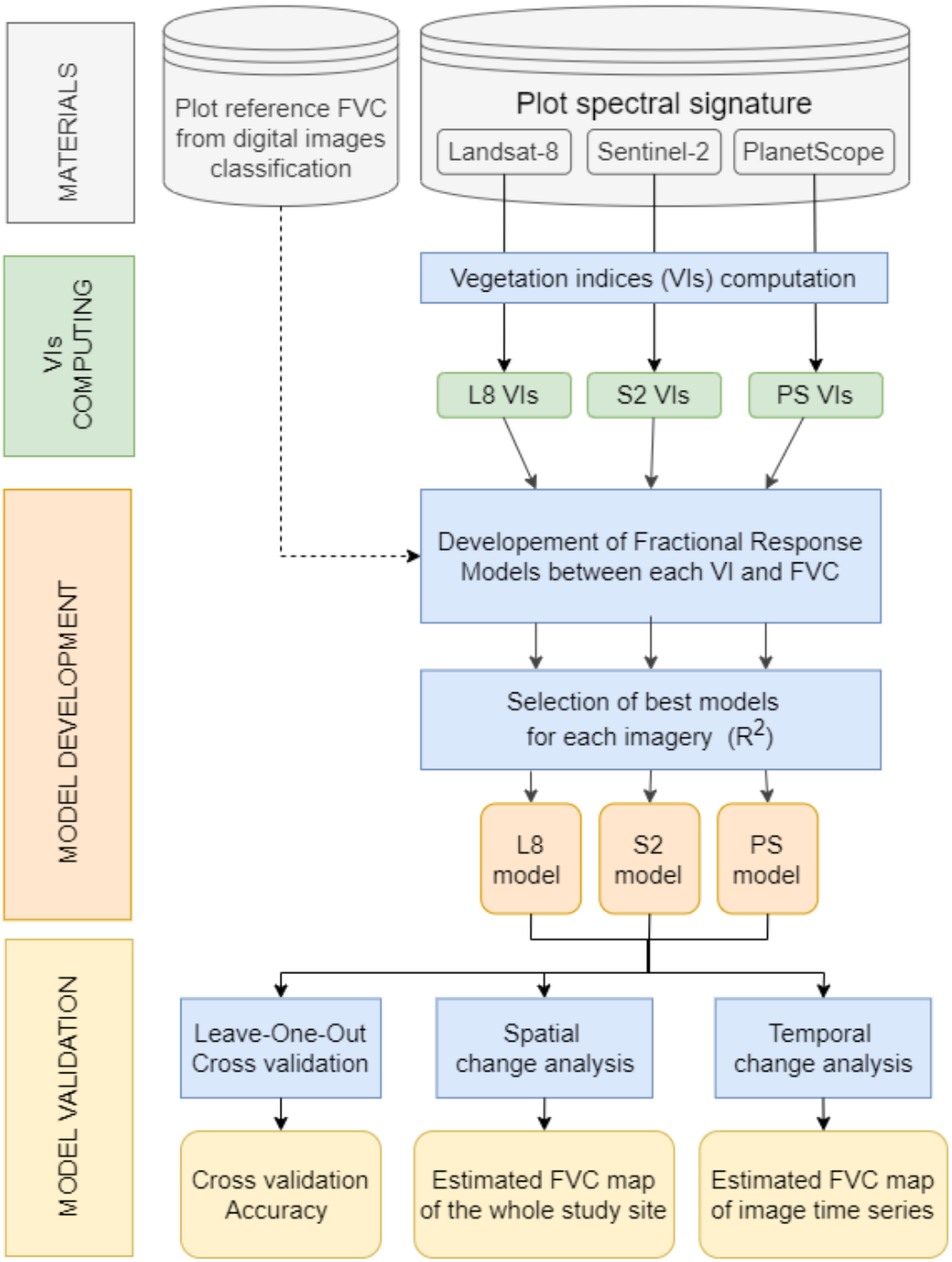


*Figure S2. Model development workflow.*

*Table S1. Product specification of the analysed images*

| Imagery | Product Level | Product available from | Acquisition date | Band specifications<br>Code (name) ~ central wavelength (spat. res.) |
|---|---|---|---|---|
| Landsat-8 | 2 | April 2013 | 13/06/2021 | SR_B1 (coastal aerosol) ~ 443 nm (30 m)<br>SR_B2 (blue) ~ 482 nm (30 m)<br>SR_B3 (green) ~ 561.5 nm (30 m)<br>SR_B4 (red) ~ 654.5 nm (30 m)<br>SR_B5 (near infrared) ~ 865 nm (30 m)<br>SR_B6 (shortwave infrared 1) ~ 1608.5 nm (30 m)<br>SR_B7 (shortwave infrared 2) ~ 2200.5 nm (30 m) |
| Sentinel-2 | 2A | March 2018 | 27/06/2021 | B1 (aerosols) ~ 443.1 nm (60 m)<br>B2 (blue) ~ 494.4 nm (10 m)<br>B3 (green) ~ 559.5 nm (10 m)<br>B4 (red) ~ 664.8 nm (10 m)<br>B5 (red Edge 1) ~ 703.9 nm (20 m)<br>B6 (red Edge 2) ~ 739.7 nm (20 m)<br>B7 (red Edge 3) ~ 781.1 nm (20 m)<br>B8 (near infrared) ~ 834.1 nm (10 m)<br>B8A (Red Edge 4) ~ 864.4 nm (20 m)<br>B9 (water vapor) ~ 944.1 nm (60 m)<br>B11 (shortwave infrared 1) ~ 1612.1 nm (20 m)<br>B12 (shortwave infrared 2) ~ 2194.1 nm. (20 m) |
| PlanetScope | 3A (PSB.SD instrument) | March 2020 | 23/06/2021 | b1 (Coastal Blue) ~ 441.5 nm (3.125)<br>b2 (Blue) ~ 490 nm (3.125)<br>b3 (Green I) ~ 531 nm (3.125)<br>b4 (Green II) ~ 565 nm (3.125)<br>b5 (Yellow) ~ 610 nm (3.125)<br>b6 (Red) ~ 665 nm (3.125)<br>b7 (Red-Edge) ~ 705 nm (3.125)<br>b8 (NIR) ~ 865 nm (3.125) |